

# Influence of field effect on the performance of InGaAs-based terahertz radiation detectors

Linas Minkevičius · Vincas Tamošiūnas ·  
Martynas Kojelis · Ernestas Žasinas ·  
Virginijus Bukauskas · Arūnas Šetkus ·  
Irmantas Kašalynas · Gintaras Valušis

Received: date / Accepted: date

**Abstract** Detailed electric characterization of high-performance bow-tie InGaAs-based terahertz detectors and corresponding simulation results are presented. The local surface potential and tunneling current were scanned on the surface of detectors by Kelvin probe force microscope (KPFM) and scanning tunneling microscope (STM) and a position of the Fermi level was obtained from these experiments. Current-voltage curves were measured and modelled using Synopsys Sentaurus TCAD package to get a better insight of processes happening within the detector. In addition, finite-difference time-domain simulations were performed to reveal the peculiarities of electric field concentration by the metal contacts of the detectors. Results of investigation confirm that field-effect induced conductivity modulation is a possible contributing mechanism to high sensitivity of the studied sensors.

**Keywords** Terahertz · Bow-tie detector · InGaAs

## 1 Introduction

The search for highly sensitive detectors operating at room temperature remains one of the top priorities in developing devices for the terahertz frequency range. Multiple concepts are being tested for such mission - Schottky detectors [1], microbolometer

---

This work was supported by the Research Council of Lithuania (project LAT 04/2016).

L. Minkevičius, V. Tamošiūnas, I. Kašalynas, G. Valušis  
Center for Physical Sciences and Technology, Saulėtekio av. 3, LT-10222 Vilnius, Lithuania  
Vilnius University, Faculty of Physics, Saulėtekio av. 9, Bld. III, LT- 10222 Vilnius, Lithuania  
Tel.: +370-5-2312418  
Fax: +370-5-2627123  
E-mail: linas.minkevicius@ftmc.lt

M. Kojelis, E. Žasinas  
Vilnius University, Institute of Applied Research, Saulėtekio av. 9, Bld. III, LT- 10222 Vilnius, Lithuania  
V. Bukauskas, A. Šetkus  
Center for Physical Sciences and Technology, Saulėtekio av. 3, LT-10222 Vilnius, Lithuania

arrays [?], semiconductor field-effect transistors (FETs) with nanometric gates [4–7], bow-tie (BT) shaped semiconductor diodes [8–10]. Recently it was demonstrated, that InGaAs based bow-tie diodes can reach 10 V/W sensitivity with  $4 \text{ nW}/(\text{Hz})^{1/2}$  noise equivalent power (NEP) in direct mode [?], 230 fW/Hz in heterodyne mode [11] and, therefore, such type of the device remains as one of the most promising candidates for direct applications at room-temperature detection schemes.

It was supposed that detection effect in bow-tie diodes relies on non-uniform carrier heating when external illumination is concentrated in semiconducting part of the diode by a metallic part of the device causing thus dc voltage over the ends of the sensor [9].

In this paper, we extend the concept of device operation illustrating that self-mixing in low-conductivity InGaAs layer can play significant role in signal formation in addition to carrier heating effects. It is revealed by presenting results of experimental investigation and numerical simulations of electrical properties of InGaAs-based THz bow-tie detectors. Kelvin probe force microscopy (KPFM) [12] and scanning tunneling microscopy (STM) were applied to measure local surface potential and tunneling current on the surface of the detectors. Based on these results, a position of the Fermi level was obtained for the studied structures. These results provided the starting parameters for the further theoretical analysis using Synopsys Sentaurus TCAD package for semiconductor devices. Finite-difference time-domain (FDTD) simulations revealed factors of electric field concentration, other antenna-related effects and highlighted the most important device areas defining the origin of the detector response.

## 2 Processing of samples

Two InGaAs samples were grown using molecular beam epitaxy and processed as already described in [11]. Parameters of the investigated samples are summarized in Table 1. A cross-section of modelled devices is depicted in Fig. 1b. Layer of 501–540 nm thick  $\text{In}_{0.47}\text{Ga}_{0.53}\text{As}$  and a monolayer of InAs (for sample II3169) were grown on 500  $\mu\text{m}$  thick InP (001) substrate. Mesas were formed using wet chemical etching. For the metallisation, a Ti layer with a thickness of 20 nm and an Au layer with thickness of approximately 180 nm were deposited as a two-layer structure. The gap between the metal contacts was set to 10  $\mu\text{m}$  during photo-lithography mask production for all samples with exception of I204 that had various gaps of up to 20  $\mu\text{m}$ . It was slightly smaller in finished devices due to processing peculiarities.

A scheme of the expected band variation across the tested structures is graphically presented in Fig. 2. They are based on several assumptions: 5.1 eV and 4.3 eV work function for gold and titanium respectively, 4.5 eV electron affinity, 0.2 eV Fermi level position below conduction band minimum and complete external electric field screening for the bottom of  $\text{In}_{0.47}\text{Ga}_{0.53}\text{As}$  and only small band bending near the surface of InGaAs in proximity of the gold contact. Applicability of the last three factors will be discussed later.

It is worth noting several main features of energy levels, sketched in Fig. 2. First, work function value of Ti is smaller than electron affinity of  $\text{In}_{0.47}\text{Ga}_{0.53}\text{As}$ , therefore,

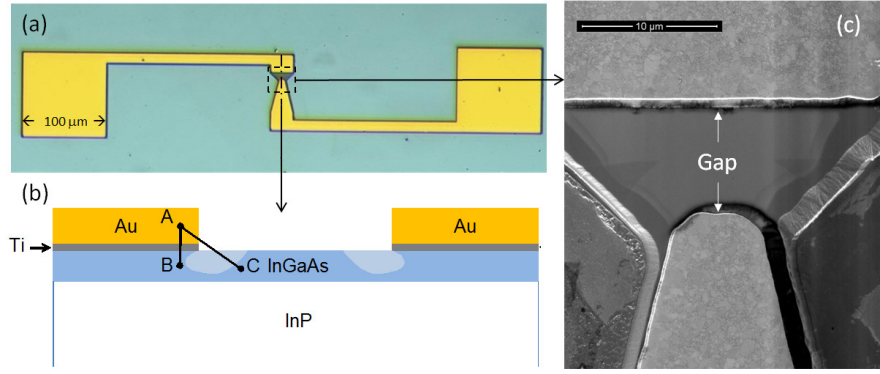


**Fig. 1** (a) Photograph of the sensor consisting of the active part with antenna (central part), bonding pads (large  $100 \times 100$  areas on the left and the right sides) and contact stripes. Dashed lines indicate the approximate positions for the cross-section sketch (b) and SEM image (c). (b) Cross-section of the modelled device (not to scale). Letters "A", "B", "C" mark the ends of cross-sections for which electrostatic analysis will be performed further. Lighter blue areas mark approximate positions of  $\text{In}_{0.47}\text{Ga}_{0.53}\text{As}$  areas in which Au contact edge might influence carrier concentration due to electrostatic effects. (c) SEM image of the active part of the sensor with indicated gap between metal contacts.

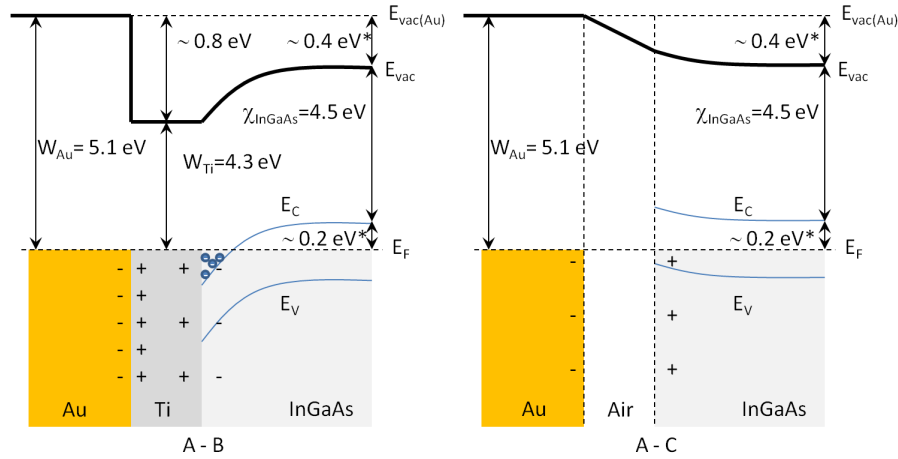


**Fig. 2** Sketch of the expected vacuum energy level (thick line) dependence on coordinate without applied external voltage. Left: along A - B line. Right: along A - C line. (\*) marks estimated values for the case of low doping and assuming no surface charge or Fermi level pinning.

potential well for electrons is formed near the interface between these two materials and ohmic contact should be formed in case of n-type  $\text{In}_{0.47}\text{Ga}_{0.53}\text{As}$ . Previous study of ohmic Ti/Pt/Au contact stability on InGaAs [13] confirmed that Ti layer on InGaAs remains stable even after annealing at  $450^\circ\text{C}$ , when contact resistance starts to degrade due to InGaAs decomposition, thus we expect that Ti/Au bilayer also stays stable in our case, and electron accumulation due to low work function of Ti mostly contributes to ohmic type behaviour in case of our contacts.

**Table 1** Description of the InGaAs samples

Sample	$t_{\text{InGaAs}}$ , nm	$x(\text{Ga})$	InAs monolayer
II3169	520	0.53	yes
I197	540	0.53	no
I204	501	0.532	no

With no external voltage, Fermi level is the same for all connected materials, therefore potential difference of the order of several hundred millivolts is expected between the gold layer and  $\text{In}_{0.47}\text{Ga}_{0.53}\text{As}$  layer areas sufficiently far away from the corner for a complete screening of electric field. Situation is more complicated in case of areas near the edge of metal contacts, since side wall of Au contact layer is located in the proximity of  $\text{In}_{0.47}\text{Ga}_{0.53}\text{As}$  layer in this area due to low thickness of Ti layer (only 20 nm). Therefore, due to the complex shape of this multilayer device, there is no analytical solution for exact potential distribution. Therefore, later described Sentaurus TCAD simulations were performed to compute numerically possible distributions of electrostatic potential for several scenarios involving different overlaps of metal layers and surface charges. Experimentally measured current-voltage (IV) curves and results of Kelvin probe measurement results served as a starting point for the initial evaluation of simulation parameters.

### 3 Electrical characterization of the samples

#### 3.1 Kelvin probe measurements

Dependence of the work function on the distance (Fig. 1) was measured using Veeco Dimension 3100/Nanoscope IVa Atomic Force Microscope. Obtained results for II3169 sample with applied 0.3 V external voltage and both samples without an external voltage are presented in Fig. 3. Note that zero coordinate corresponds to the edge of the narrower metal contact. This contact also serves as 0 meV reference for the measurements. Device with 19  $\mu\text{m}$  gap was measured in case of sample I204. Due to limitations of available 10  $\mu\text{m}$  scanning range in our set-up, two scans need to be performed.

As one can clearly see from Fig. 3, work function difference gradually raises within first 1  $\mu\text{m}$  from the metal edge reaching approximately 0.4 eV and > 0.2 eV difference in comparison with the gold surface in case of samples I204 and II3169, correspondingly. At the same time, much smaller potential differences are observed for sample I197. A sketch of expected results based on Fig. 2 is also depicted in this figure. One can easily observe the difference of at least several hundreds meV in the centre between the contacts. Such a large difference could either suggest that Fermi level is located several hundred meV lower than initially estimated, or that observed results are influenced by additional factors such as surface states and surface charges.

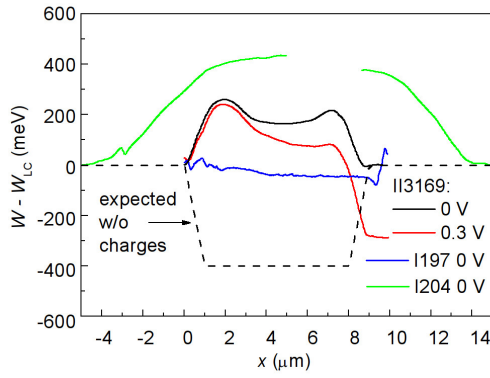


**Fig. 3** Work function dependence on distance between the metal contacts of the BT detectors. Solid lines - KPFM measurement results, dashed line - sketch of the expected (without the influence of surface charges) dependence based on Fig. 2. Work function of the left contact served as a reference value for this graph. The edge of the left contact is located at  $x \approx 0 \mu\text{m}$  coordinate for samples II3169, I197 and  $x \approx -5 \mu\text{m}$  for sample I204. The right edge of the contact is located at  $x \approx 9 \mu\text{m}$  coordinate for samples II3169, I197 and  $x \approx 14 \mu\text{m}$  for sample I204. Two measured dependences are presented for the samples II3169 - with 0.3 V bias voltage (red line) and without it (black line). Two separate measurements were performed for the sample I204, since the gap size ( $19 \mu\text{m}$ ) exceeded the maximum available scanning range of our setup.

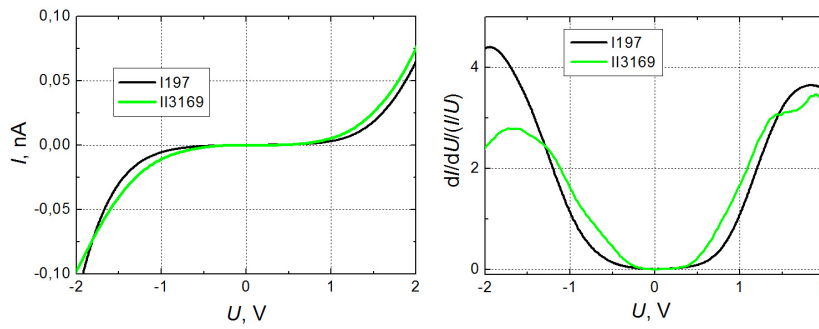


**Fig. 4** Dependence of the tunneling current (left) and its derivative (right) on the sample bias.

### 3.2 Scanning tunneling spectroscopy measurements

Surface Fermi level position and surface density of states (SDOS) were also evaluated by means of scanning tunnelling spectroscopy (STS) technique in the same set-up in order to supplement previously presented KPFM measurements. Results of these measurements are presented in Fig. 4. As one can see from this figure, normalized derivative of the tunnelling current (and, at the same time, surface density of states) starts increasing at approx. 0.4 V and - 0.3 V. Difference between these voltages is consistent with the bandgap of InGaAs sample and voltages corresponding to higher SDOS regions indicates that Fermi level is located only slightly below the middle of the bandgap.

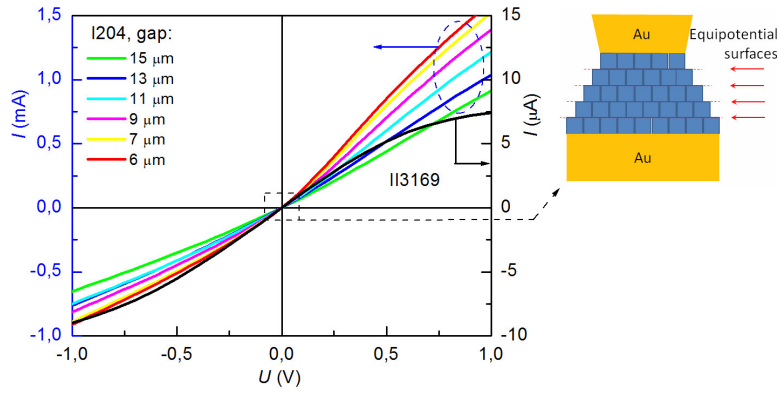


**Fig. 5** Left: IV curves of the samples. Note the scale difference. Dotted black rectangle indicates part of the IV, which was used for estimating the averaged carrier concentration. Right: illustration of the model used to relate the differential resistance of the sample to square sample resistance of the layer - area of the active part of the sensor was filled with small squares. Resistances were calculated assuming equipotential borders between the rows of squares and parallel connection within these rows.

The difference of 0.4 eV between Fermi level and the bottom of the conduction band with 4.5 eV electron affinity would lead to approximately 4.9 eV work function, so the missing several hundred meV have to be found for sample II3169 to explain the work function dependence on coordinate in Fig. 3.

Similar difference of several hundred meV between STS and KFPM results was already noticed previously with InGaAs and attributed to a fixed charge of  $7.3 - 12 \times 10^{12} \text{ cm}^{-2}$ , shifting of Fermi level in case of KFPM and much lower sensitivity of STS to surface charges [12]. Since comparable differences between STS and KFPM results are obtained in case of our samples, we will employ similar values of surface charge in our simulations presented later.

### 3.3 Measurements of current-voltage characteristics

Current-voltage characteristics (IVs) of the investigated samples are presented in Fig. 5. Two major features are apparent: difference of nearly two orders of magnitude between differential resistances at 0 V point (slope of the curves is similar, however, current values of the left and the right scale differ by two orders of magnitude) and IV curve bending for the sample with higher resistance once voltage approaches the value of 1 V. Note that IVs of the sample II3169 are similar to the characteristics of typical BT diode presented in [?]. Voltage of 1 V, averaged across approximately 10  $\mu\text{m}$  gap between the metal contacts, translates to the average electric field of 1 kV/cm. By taking into account the shape of the device, one could estimate the 2.5 kV/cm maximum electric field value near the tip of the narrower metal contact using a simplified model presented in the next paragraph and Fig. 5. This value is of the same order, but still smaller than approx. 3 kV/cm, at which negative-differential-mobility is expected to manifest itself [14]. Therefore, IV linearity of sample I204 up

to 1 V is not surprising even with slight gap variation (Fig. 5). For sample II3169, however, IV curve bending is already observed at 0.5 V, so one has to look for additional factors, such as field effect due to surface charges or edges of the metal contact which might lead to additional field non-uniformity within the InGaAs layer.

Due to the shape of the sample, resistance  $R$  of the sample (in  $\Omega$ ) is expected to be approximately 80 % of sheet resistance of the layer  $R_{sq}$  (in  $\Omega/\text{sq}$  units). This approximate value is evaluated by meshing the shape of the active area of the device into rows square cells. Further, the resistance assuming parallel electrical connection within lines and serial - between them, as illustrated on the right part of Fig. 5 was calculated. In this case,  $R \approx 100 \text{ k}\Omega$  measured differential resistance of the sample II3169 with expected  $\mu = 9 \times 10^3 \text{ cm}^2/\text{V}\cdot\text{s}$  electron mobility, leads to  $n = 7 \cdot 10^{13} \text{ cm}^{-3}$  averaged concentration estimation for 0.5  $\mu\text{m}$  InGaAs layer thickness. This value with the expected intrinsic carrier density  $n_i = 6.3 \cdot 10^{11} \text{ cm}^{-3}$  [15] and leads to approximately 0.2 eV difference between the bottom of InGaAs conduction band and Fermi level. This value was used for sketching the energy levels further away from the metal contact in right part of Fig. 2. As it was mentioned earlier, this model also provides an estimation of the 2.5 ratio between the maximum and the average electric field values. However, this value should be treated as an absolute upper limit due to imperfection of the used model - current spreading without potential differences are assumed in the lateral direction.

However, in fully depleted InGaAs layer approximation, assuming zero electric field strength near the bottom of InGaAs layer,  $N_D = n = 7 \times 10^{13} \text{ cm}^{-3}$  concentration of ionized donors,  $t_{\text{InGaAs}} = 534 \text{ nm}$  thickness of the channel and  $\epsilon = 13.9$  relative dielectric permittivity, one could apply usual calculation procedure for field-effect transistor (FET) channel pinch-off and estimate a potential difference required for a full depletion between the bottom and the top of the layer based on Gauss's law:

$$\Delta\phi_{\text{PO}} = \int_0^{t_{\text{InGaAs}}} q_0 \times N_D \times \frac{z}{\epsilon\epsilon_0} \times dz = q_0 \times N_D \times \frac{t_{\text{InGaAs}}^2}{2\epsilon\epsilon_0} \approx 13 \text{ mV}. \quad (1)$$

A corresponding value of electron potential energy difference (13 meV) is more than one order of magnitude smaller than work function differences between experimentally measured values and expected ones (see Fig. 3), hence, one can expect that surface charges might play a crucial role defining the electrical properties of our sensors. At least partial depletion of the layers might also mean, that an apparent averaged carrier concentration is substantially lower than the actual dopant concentration.

Therefore, later presented comprehensive Sentaurus TCAD IV simulations with the same or higher doping levels and partially depleted by surface charges InGaAs layers were performed to reveal the conditions for reduced differential conductance observed at voltages approaching  $\pm 1 \text{ V}$  (Fig. 5) for the sample II3169.

#### 4 IV simulation results

IV simulations using Sentaurus TCAD [16] were performed in order to reveal possible phenomena leading to observed experimentally IV curves. Since low apparent

conductivity of the samples correlate with current limitation in the IV curves, which is similar to output IVs of field-effect (FET) transistors, including ones previously used for sub-terahertz detection [17] two main factors possibly appearing as a result of device fabrication were considered.

The first one is the Au layers overlap over Ti sublayers possibly taking place during gold deposition process. At the places of overlaps Au layers have tiny interfaces with InGaAs channel around Ti contact sublayers. As a result of larger workfunction of Au (5 eV) than the one of Ti (4.3 eV) the Schottky barriers are formed around Ti contact sublayers thus impeding the movement of electrons from one Ti contact sublayer to another upon application of voltage.

The second feature which may affect the character of IV curves is the surface charge appearing at the top surface of InGaAs channel between the contacts. The negative surface charge (expected from Kelvin probe measurements) creates the negative electrostatic potential forcing electrons to move away from InGaAs surface and reducing the thickness of the conductive part of the channel.

Both these technological aspects could facilitate the formation of charge depletion regions within the InGaAs channel and act effectively like a gate in FET device.

In addition, we paid special interest to the mobility of electrons in our simulations. The values of electric field present in the studied devices are large enough to affect the charge mobility. Therefore, we separately studied the high-field depending mobility effect on the shape of IV curves presented later in the paper.

Material parameters for the device simulation were taken from the Sentaurus TCAD material database library. The parameter data file for  $\text{In}_{0.47}\text{Ga}_{0.53}\text{As}$  was created once for the given molecular fraction as prescribed in [18]. In the obtained parameter file we explicitly modified low field electron mobility value according to various literature sources disabling in the same time the default model for mobility dependence on doping. The mobility values used in our simulations are presented in the Table 2. Several simulations for high electric fields were also performed with modified mobility values as it will be explained in the subsection below. Other parameters of InGaAs and of the rest of materials were unchanged.

**Table 2** Mobility values used in our simulations

Doping concentration ( $\text{cm}^{-3}$ )	Mobility ( $\text{cm}^2\text{V}^{-1}\text{s}^{-1}$ )	Source
$1 \cdot 10^{14}$	16000	TCAD database
$9 \cdot 10^{14}$	10000	[14]
$1 \cdot 10^{15}$	10000	same as for $9 \cdot 10^{14}$
$2.9 \cdot 10^{15}$	8500	[14]
$4 \cdot 10^{16}$	7000	[19]
$2.3 \cdot 10^{17}$	6000	[19]

Physical models used in simulations were the following: Fermi statistics at  $T = 300$  K; hydrodynamic transport for electrons and holes; mobility high-field saturation either with hydrodynamic driving force (high-field effect disabled) or with charge driving force given by the gradient of quasi-fermi potential (high-field effect enabled); recombination models were the Shockley-Read-Hall, the radiative and



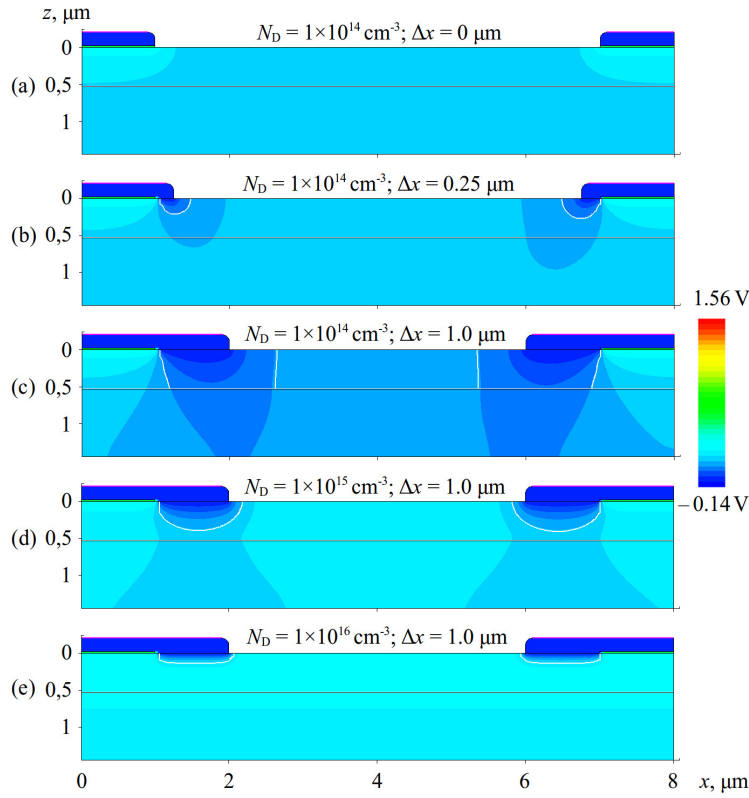


**Fig. 6** Distribution of the electrostatic potential in cross section of the device: for fixed  $N_D = 1.0 \times 10^{14} \text{ cm}^{-3}$  doping and variable 0-1.0  $\mu\text{m}$  overlap of Au contact and InGaAs (a-c); for fixed 1.0  $\mu\text{m}$  overlap of Au contact and InGaAs and variable  $N_D = 1 \times 10^{14 \div 16} \text{ cm}^{-3}$  doping (c-e).

the Auger. The Schottky barrier models were specified at the Titanium-InGaAs and Gold-InGaAs interfaces.

Two contacts were declared on the top of each golden layer. The boundary conditions were set by the contacts voltages being 0 V on one contact and the variable voltage on the other.

The simulated device has a two-dimensional geometry shown in the Fig. 1.b). Specified layer thicknesses were: InP layer - 1  $\mu\text{m}$ , InGaAs layer - 0.536  $\mu\text{m}$ , each titanium contact sublayer - 20 nm, each golden contact layer - 100 nm. The 0.1  $\mu\text{m}$  thick air layer on top of the device was useful for correct definition of the surface charge at the InGaAs / Air interface. Length of the entire simulation area was set to 8  $\mu\text{m}$ .

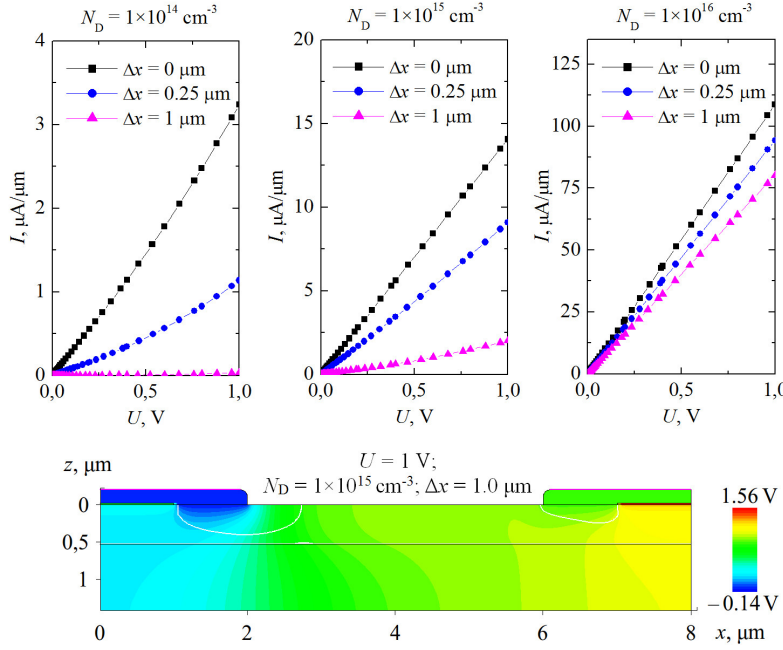


**Fig. 7** Top: simulated IV curves for several doping levels and overlaps of metal contacts. Bottom: distribution of electrostatic potential within the device in case of 1 V sample bias, 1.0  $\mu\text{m}$  overlap and  $N_D = 1.0 \times 10^{15} \text{ cm}^{-3}$  doping.

#### 4.1 Influence of contact overlaps and surface charges on IV characteristics

First electrostatic (with zero applied external voltage) simulations were attempted with variable metal overlap and with variable semiconductor doping as another parameter. These simulation results are summarized in Fig. 6. As one can see, at a fixed doping of  $N_D = 1.0 \times 10^{14} \text{ cm}^{-3}$  (panels (a)-(c)), Schottky barrier and depleted region (boundaries are tentatively indicated by white lines) are formed below gold contact due to relatively high work function of gold. This depleted region covers an entire channel once an overlap is increased to 1.0  $\mu\text{m}$ . At higher doping levels, as expected, size of this depleted region is reduced due to higher density of charges and therefore - screening of the electrostatic fields by thinner charged layers.

Results at higher doping levels offer possibility to explain experimentally measured IVs (Fig. 5) - open channel and high carrier concentration would lead to ohmic-like behaviour at low voltages. At lower doping, FET-like current limiting is expected once channel is closed by depleted region. However, such simplified analysis is obstructed by the fact that InGaAs layer thickness is of the same order as metal thickness and radius of the curvature near the edge, thus short channel type transistor operation and full numerical simulation has to be considered.

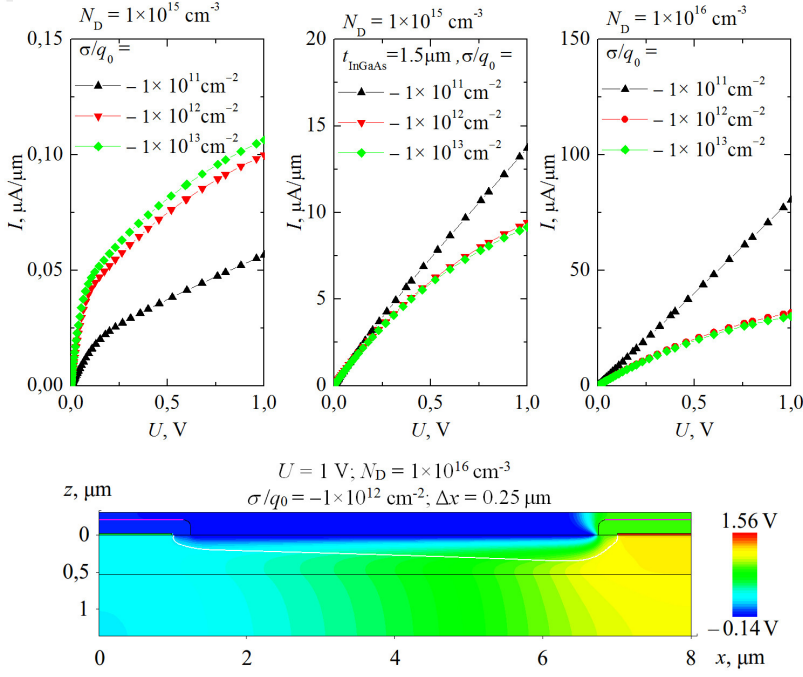


**Fig. 8** Top: simulated IV curves for several doping levels and surface charge densities. Bottom: distribution of electrostatic potential within the device in case of 1 V sample bias, 0.25  $\mu\text{m}$  overlap,  $N_D = 1.0 \times 10^{16} \text{ cm}^{-3}$  doping and  $\sigma = -1.0 \times 10^{12} q_0 \times \text{cm}^{-2}$  surface charge density.

Results for several metal overlaps and doping concentrations are presented in Fig. 7. As one can clearly see, bending observed in Fig. 5, is not visible here. In contrary, in some cases IVs even bend upwards. Such results confirm previously expressed reservations about Schottky-type gate, obtained using just metal overlap. An additional problem is illustrated in the bottom panel of Fig. 7. Once sample bias is increased, thickness of depleted region grows near one of the metal contacts, channel width is reduced there and the largest potential drop is obtained near this contact. This contradicts somewhat with our previously presented in Fig. 3 results, where rather gradual drop of the additional potential difference is observed.

These both factors lead to a further model refinement - possible influence of surface charges of the open InGaAs surface was considered in order to numerically simulate larger (along  $x$  axis) partially depleted InGaAs area. Several experimental results place reasonable starting estimations of their values and on the doping values. On one hand, even without current limitation by complete depletion, average doping of at least  $N_D = 1.0 \times 10^{15} \text{ cm}^{-3}$  order is required (as illustrated in Fig. 7) to obtain the experimental values of the current presented in Fig. 5.

Several simulation results looking closest to FET type of IV are presented in Fig. 8. As one can clearly see, introduction of relevant surface charges leads to the

required IV curve shape bend. However the parametrical dependence of IV curves shape has significantly different character which is defined both by the value of doping and the width of the InGaAs channel. For the fixed width of the channel and high doping levels (top right panel in Fig. 8) the larger surface charge decrease the value of current. This is because the depletion region below the InGaAs / Air interface is widened with the increasing charge and the conductivity of the channel is effectively decreased. (For the  $N_D = 1.0 \times 10^{16} \text{ cm}^{-3}$  doping Debye screening length in InGaAs is  $0.05 \text{ } \mu\text{m}$  and the depletion region width is  $0.1 - 0.15 \text{ } \mu\text{m}$  for the given surface charge values.) It is not in the case of lower doping for the same width of the channel (top left panel in Fig. 8). The values of current are by two orders lower in the presence of the surface charge (compare values of current with the ones without charge in the Fig. 7 top middle panel blue curve) and the current itself increases with the increased surface charge. Such a different behavior of IV curves takes place when the depletion region width becomes equal or larger than the width of InGaAs channel. (In case of  $N_D = 1.0 \times 10^{15} \text{ cm}^{-3}$  doping Debye screening length in is  $0.14 \text{ } \mu\text{m}$  and the depletion region width is  $0.4 - 0.5 \text{ } \mu\text{m}$  for the given surface charge values.) In such a situation the major carriers (electrons) dramatically loose their role in the total current and the parametrical increase of current takes place due to the increasing values of minor carriers concentration (recall that the electrons and holes concentration product is constant due to acting mass law). However for the same doping level situation changes if the InGaAs channel width is enlarged to be wider than the depletion region. As shown in top middle panel in Fig. 8 the parametric IV dependencies for the device with the thicker InGaAs channel are the same for both doping levels.

The order of obtained current values is lower than expected from the experimental data at  $N_D = 1.0 \times 10^{15} \text{ cm}^{-3}$  doping and higher at  $N_D = 1.0 \times 10^{16} \text{ cm}^{-3}$  doping. However, both these values are higher than estimated average one (Ch. 3.3,  $N_D = 7.0 \times 10^{13} \text{ cm}^{-3}$ ) due to partial channel depletion.

#### 4.2 Influence of high-field-effects

Since our simulation results revealed substantial carrier density and electrostatic variations in a vertical (perpendicular to an unetched InGaAs surface) direction, more comprehensive models were included in our simulations, leading to results presented in Fig. 9.

High-field mobility dependence model used in TCAD by default is referred to as Canali model [20] which originates from the Caughey–Thomas formula [21]:

$$\mu(F) = \frac{(\alpha + 1)\mu_0}{\alpha + \left[1 + \left(\frac{(\alpha+1)\mu_0 F}{v_{sat}}\right)^\beta\right]^{1/\beta}}. \quad (2)$$

Here  $\mu_0$  is the low-field mobility,  $v_{sat}$  electron saturation velocity,  $F$  is the charge carriers driving force which is the absolute value of electric field in the simplest case and the absolute value of the gradient of quasi-fermi potential used in our calculations. The parameters  $\alpha$  and  $\beta$  are used for finer fitting of experimental data. The dependence  $\mu(E)$  for  $\text{In}_{0.47}\text{Ga}_{0.53}\text{As}$  was obtained by fitting experimental data reported

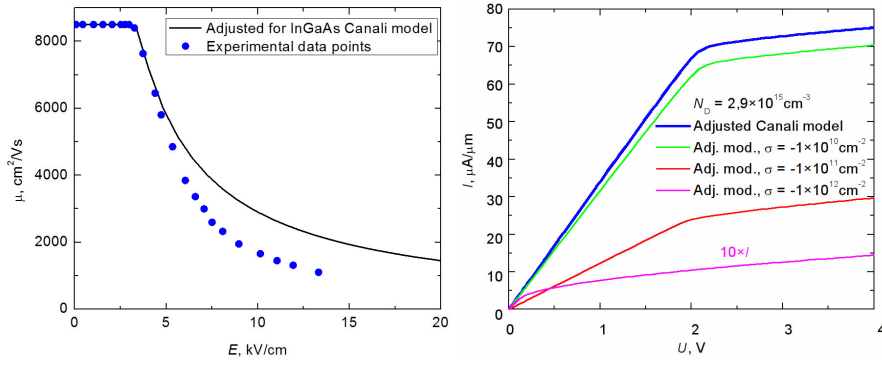


**Fig. 9** (Left) Dependence of carrier mobility on electric field for two models used in our calculations and key experimental data for comparison (after [14]). (Right) IV simulations results for build-in into TCAD Canali et. al. model [20] and adjusted model with and without surface charges.

in [14] with the formula (2). The fitting procedure result is shown in Fig.9 (left) with the following parameters:  $\mu_0 = 8500 \text{ cm}^2\text{V}^{-1}\text{s}^{-1}$ ,  $v_{sat} = 2.9 \cdot 10^7 \text{ cm/s}$ ,  $\alpha = 0$  and  $\beta = 40$ .

Modifications of built-into TCAD Canali et al. model were used to specify the dependence of mobility on the electric field as presented in the left panel of Fig. 9. First, value of maximum mobility was adjusted to match InGaAs. Afterwards, model was further adjusted to ensure a constant mobility up to 3 kV/cm. Key experimentally obtained points from [14] are also presented for comparison purposes.

Several simulation results, obtained with these mobility models, are presented on the right panel of Fig. 9. As one can clearly see, negative differential resistance at high fields above 3 kV/cm is not sufficient to justify the experimentally observed VI shape of sample with higher resistance. Linear current growth is restricted at below 1 V voltages only for the largest surface charge, when current values are already substantially reduced due to field effect.

## 5 FDTD simulations

After the model for DC current-voltage characteristics is established and suitable ranges of parameters are defined, one can turn to high frequency AC models. Finite-difference time-domain simulations were performed to reveal the expected distributions of electric field amplitudes near the metal tips. Obtained distribution of electric field amplitude within InGaAs detector is presented in Fig. 10. As one can clearly see, electric field is mainly concentrated near the edge of the sharper metal contact. This AC field acts as a high frequency voltage source between the gate and source of the equivalent FET. Vertical electric field component  $E_y$  is responsible for modulation of channel conductivity. AC current induced by  $E_x$  in-plane field component is therefore partially rectified to produce an observable DC component. The second transistor on the other side of device is also acting as a FET detector, however, its influence is reduced due to much lower electric field amplitudes. Such detection mechanism has

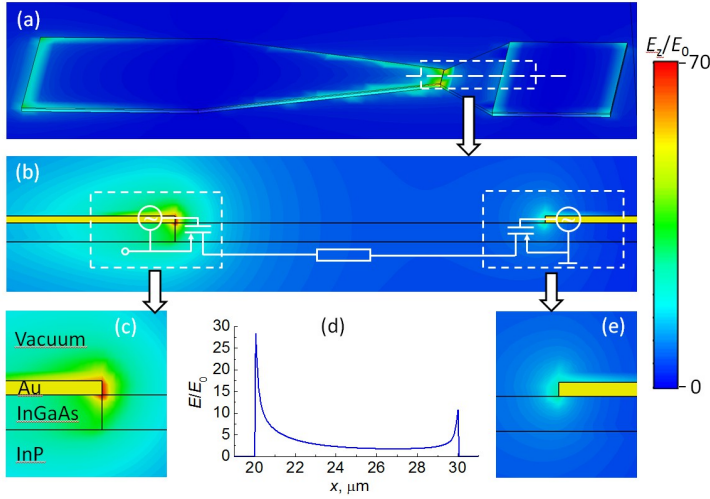


**Fig. 10** Distributions of electric field amplitude within the detector at 0.6 THz (a); enlarged part of the top panel and a sketch of equivalent circuit (b); distribution of electric field amplitude near metal contact edges (c,e) and the dependence of amplitude on the coordinate along the symmetry axis of the active part (d). Dashed lines indicate an approximate location of areas to be enlarged in the following panels of the figure.

similarities with recently demonstrated one for junctionless FETs [22]. However, in our case, the edge of the metal contact acts as a compact gate, while an equivalent of DC gate-source voltage would be "provided" by metal work function differences and open surface charges.

## 6 Influence of DC current on detector's sensitivity

Several important detector properties can be expected based on simulation results presented in Sections 4 and 5. First, if channels of both "FET-like" device parts are indeed partially conductive without applied external voltage (as expected from IV's of Fig. 5) and if potential reduction of the corresponding metal electrode can "squeeze" selectively one of them (as expected from Fig. 7), one would expect a possibility of tuning of resistive self-mixing performance of both "FET-like" parts by changing applied DC voltage. Also, both "FET-like" parts are connected in series and would produce rectified voltage of opposite signs. As a result, so the voltage of the rectified signal should change sign when switching from pick-off of one "FET" to another. For DC voltages between these two regimes, detector signal should change gradually and reach zero for equal contributions of both parts of the device.

### 6.1 Experimental data

To experimentally verify these assumptions, one of bow-tie devices was connected to a programmable Keithley 2400 sourcemeter through serially connected  $0.47 \text{ M}\Omega$

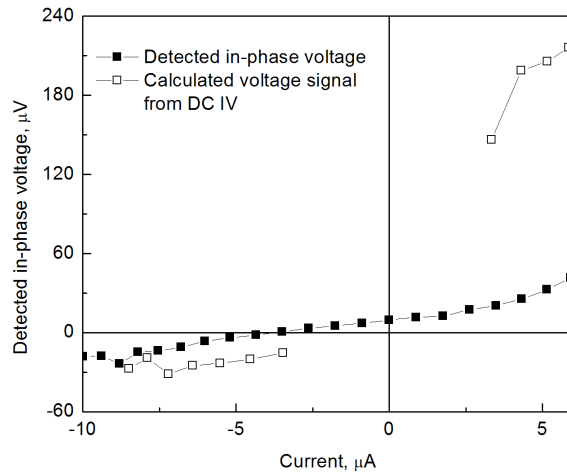


**Fig. 11** Dependence of the calculated and experimentally detected signal on applied DC bias voltage. Frequency multiplier chain, operating at 0.584 THz served as THz source with its output modulated at 1 kHz by an external function generator. Signal Recovery 7265 lock-in amplifier, operating with 10 s integration time was used to analyse the output signal.

resistors. Detector was illuminated by focused 0.584 THz wave from VDI MC156 frequency multiplier chain fed from Agilent E8257D synthesizer. Amplitude of the incident THz wave was modulated by TTL-compatible signals from Agilent 33500B function generator, providing complete on-off modulation. AC signal from the detector was collected using Signal Recovery 7265 lock-in amplifier operating at 10s integration time. Both in-phase and out-of-phase signals were recorded using PC connection of the lock-in amplifier. Obtained results are presented in Fig. 11. As expected, sign of the in-plane voltage signal changes at approximately  $-3.5 \mu\text{A}$  when increased resistive self-mixing performance of the "wider-FET" compensates the influence of better electric field concentration (illustrated in Fig. 10) within the narrower one.

## 6.2 Theoretical evaluation

Electric field amplitude distributions (Fig. 10 (d)) together with IV curve of Fig. 5 also present an opportunity to evaluate if our experimentally recorded signal levels do not exceed the ones which could be expected from the non-linearity of IV curve.

Assuming that 0.8 mW power of THz beam is focused to the spot of approx. one wavelength ( $\approx 500 \mu\text{m}$ ) diameter, one can get an estimation of irradiance of  $4 \text{ kW/m}^2$  in a focus spot. This translates into  $E_0 \approx 1.7 \text{ kV/m}$  electric field amplitude.

All simulated electric field amplitude values in Fig. 10(d) were normalized to  $E_0$ , so these results can be applied to evaluate an equivalent source-gate voltage for each of the FETs of Fig. 10(b). By integrating electric field within  $2 \mu\text{m}$  from the edge of the metal contacts (located at  $x_1 = 20 \mu\text{m}$  and  $x_2 = 30 \mu\text{m}$ ), one can get AC voltage

amplitude values of approx.  $U_{AC1} = 15 \times E_0 \times 1 \mu\text{m}$  and  $U_{AC2} = 6 \times E_0 \times 1 \mu\text{m}$  or 26 mV and 10 mV for the narrower and the wider contact, respectively.

If one assumes, that an increased non-linearity of the IV curve of the sample II3196 in a vicinity of 5  $\mu\text{A}$  DC current is caused by a pinch-off of either of transistor channel, it should be possible to evaluate the rectified current  $I_{rect}$  from these voltages:

$$I_{rect} = \frac{1}{2} \times \frac{\partial^2 I}{\partial U^2} \times \frac{U_{AC}^2}{2}. \quad (3)$$

Voltage signal, which could be obtained on  $R \approx 100 \text{k}\Omega$  resistor then would simply be:

$$U_{rect} = R \times I_{rect}. \quad (4)$$

Results of these calculations are presented in Fig. 11. Substantially larger than experimentally obtained values confirm that amplitudes of concentrated near the apex of the device electric field are more than sufficient for generation of the experimentally observed signals in a case of resistive self-mixing model in dual-FET equivalent circuit.

## 7 Conclusions

Kelvin probe force microscope (KPFM) and scanning tunneling microscope (STM) measurements of InGaAs surface work-function dependence on position revealed values shifted by up to 0.8 eV from the expected ones. Such result is consistent with the influence of the substantial surface charge. Measured voltage-current (I-V) characteristics of InGaAs-based bow-tie detectors revealed a substantial reduction of differential conductivity for samples with highest resistivity for voltages exceeding 0.5 V. Our numerical simulations confirmed that similar non-linearity of IV curves can be obtained due to surface charges of approximately  $-(10^{11} \div 10^{12}) \times q_0 \text{ cm}^{-2}$  together with a partial overlap Au layer with InGaAs. In such conditions, InGaAs layer would be at least partially depleted and the conductivity of the remaining channel could potentially be influenced by the edges of the metal contacts, acting equivalently to gates of field-effects transistors (FETs). Measured under THz irradiation dependence of the sensors output voltage on DC current confirms that this voltage indeed changes sign as expected from such dual-FET model. Finite-Difference Time-Domain simulation results together with the analysis of non-linearity of the IV curve confirmed, that induced by THz wave voltage amplitudes are sufficient to produce the output signals expected from such dual-FET structure switching from the pinch-off of one transistor to another. All these factors confirm that previously suggested hot-electron based operation model of bow-tie detectors has to be additionally updated by accounting FET-like resistive self-mixing in case of low-conductivity InGaAs.

**Acknowledgements** Authors would like to thank Dr. K. Köhler (Fraunhofer-Institut fuer Angewandte Festkoerperphysik, Freiburg, Germany) and Dr. R. Butkutė (Center for Physical Sciences and Technology, Vilnius, Lithuania) for InGaAs samples.



## References

1. T. Yasui, A. Nishimura, T. Suzuki, K. Nakayama, S. Okajima, Review of scientific instruments **77**(6), 6102 (2006)
2. I. Kašalynas, et al., in *Proc. of the 38th Internat. Conf. on Infrared, Millimeter and Terahertz Waves IRMMW-THz* (2013), pp. 8–5
3. A.W. Lee, Q. Hu, Opt. Lett. **30**(19), 2563 (2005). DOI 10.1364/OL.30.002563. URL <http://ol.osa.org/abstract.cfm?URI=ol-30-19-2563>
4. W. Knap, Y. Deng, S. Rumyantsev, J.Q. Lü, M.S. Shur, C.A. Saylor, L.C. Brunel, Applied Physics Letters **80**(18), 3433 (2002). DOI <http://dx.doi.org/10.1063/1.1473685>. URL <http://scitation.aip.org/content/aip/journal/apl/80/18/10.1063/1.1473685>
5. R. Taub, F. Tepe, S. Boubanga, D. Coquillat, W. Knap, Y.M. Meziani, C. Gallon, F. Boeuf, T. Skotnicki, C. Fenouillet-Beranger, D.K. Maude, S. Rumyantsev, M.S. Shur, Applied Physics Letters **89**(25), 253511 (2006). DOI <http://dx.doi.org/10.1063/1.2410215>. URL <http://scitation.aip.org/content/aip/journal/apl/89/25/10.1063/1.2410215>
6. S. Boppel, A. Lisauskas, M. Mundt, D. Seliuta, L. Minkevicius, I. Kasalynas, G. Valusis, M. Mitten-dorff, S. Winnerl, V. Krozer, H.G. Roskos, IEEE Transactions on Microwave Theory and Techniques **60**(12), 3834 (2012). DOI 10.1109/TMTT.2012.2221732
7. A. Lisauskas, U. Pfeiffer, E. Öjefors, P.H. Bolivar, D. Glaab, H.G. Roskos, Journal of Applied Physics **105**(11), 114511 (2009). DOI <http://dx.doi.org/10.1063/1.3140611>. URL <http://scitation.aip.org/content/aip/journal/jap/105/11/10.1063/1.3140611>
8. D. Seliuta, E. Širmulis, V. Tamošiūnas, S. Balakauskas, S. Ašmontas, A. Sužiedėlis, J. Gradauskas, G. Valušis, A. Lisauskas, H. Roskos, K. Köhler, Electronics Letters **40**, 631 (2004). URL [http://digital-library.theiet.org/content/journals/10.1049/el\\_20040412](http://digital-library.theiet.org/content/journals/10.1049/el_20040412)
9. D. Seliuta, I. Kašalynas, V. Tamošiūnas, S. Balakauskas, Z. Martūnas, S. Ašmontas, G. Valušis, A. Lisauskas, H. Roskos, K. Köhler, Electronics Letters **42**, 825 (2006). URL [http://digital-library.theiet.org/content/journals/10.1049/el\\_20061224](http://digital-library.theiet.org/content/journals/10.1049/el_20061224)
10. I. Kasalynas, D. Seliuta, R. Simniskis, V. Tamosiunas, K. Kohler, G. Valusis, Electronics Letters **45**(16), 833 (2009). DOI 10.1049/el.2009.0336
11. L. Minkevicius, V. Tamošiūnas, I. Kašalynas, D. Seliuta, G. Valušis, A. Lisauskas, S. Boppel, H.G. Roskos, K. Köhler, Applied Physics Letters **99**(13), 131101 (2011). DOI <http://dx.doi.org/10.1063/1.3641907>. URL <http://scitation.aip.org/content/aip/journal/apl/99/13/10.1063/1.3641907>
12. W. Melitz, J. Shen, A.C. Kummel, S. Lee, Surface Science Reports **66**(1), 1 (2011)
13. J. Wu, C. Chang, K. Lin, E. Chang, J. Chen, C. Lee, Journal of electronic materials **24**(2), 79 (1995). DOI 10.1007/BF02659625. URL <http://dx.doi.org/10.1007/BF02659625>
14. V. Balynas, A. Krotkus, A. Stalnionis, A. Gorelionok, N. Shmidt, J. Tellefsen, Applied Physics A **51**(4), 357 (1990). DOI 10.1007/BF00324321. URL <http://dx.doi.org/10.1007/BF00324321>
15. S. Paul, J.B. Roy, P.K. Basu, Journal of Applied Physics **69**(2), 827 (1991). DOI <http://dx.doi.org/10.1063/1.348919>. URL <http://scitation.aip.org/content/aip/journal/jap/69/2/10.1063/1.348919>
16. <http://www.synopsys.com/tools/tcad/Pages/default.aspx>
17. F. Tepe, W. Knap, D. Veksler, M.S. Shur, A.P. Dmitriev, V.Y. Kachorovskii, S. Rumyantsev, Applied Physics Letters **87**(5), 052107 (2005). DOI <http://dx.doi.org/10.1063/1.2005394>. URL <http://scitation.aip.org/content/aip/journal/apl/87/5/10.1063/1.2005394>
18. Sentaurus device user guide, version k-2015.06, Mountain View, California: Synopsys, Inc., 2015: Chapter 2, section "Physical model parameters".
19. D. Chattopadhyay, S.K. Sutradhar, B.R. Nag, Journal of Physics C: Solid State Physics **14**(6), 891 (1981). URL <http://stacks.iop.org/0022-3719/14/i=6/a=014>
20. C. Canali, G. Majni, R. Minder, G. Ottaviani, Electron Devices, IEEE Transactions on **22**(11), 1045 (1975)
21. R. Thomas, Proceedings of the IEEE **55**(12), 2192 (1967)
22. J. Marczewski, W. Knap, D. Tomaszewski, M. Zaborowski, P. Zagrajek, Journal of Applied Physics **118**(10), 104502 (2015). DOI <http://dx.doi.org/10.1063/1.4929967>. URL <http://scitation.aip.org/content/aip/journal/jap/118/10/10.1063/1.4929967>